SPACE Conferences and Exposition
13 - 16 September 2016, Long Beach, California
AIAA SPACE 2016

Aerodynamics of the RANGE Nanosatellites from Direct Flowfield Simulation

Kenneth A. Hart,* Brian C. Gunter,† and Robert D. Braun‡
Georgia Institute of Technology, Atlanta, GA, 30332-0150, USA

One of the objectives of the RANGE mission is to perform relative navigation using differential aerodynamics. The aerodynamic force coefficients, moment coefficients, and heating can be computed numerically, though this process is too computationally expensive to integrate directly into an orbit propagator. A surrogate model is developed to improve the modeling fidelity beyond a simple sphere or plate model without significantly increasing computational cost. The training points for this model come from an industry standard code for Direct Simulation Monte Carlo analysis. Detailed discussions of model development, validation, and results are included.

Nomenclature

C	Coefficient, see subscripts
CFD	Computational fluid dynamics
DAC	DSMC Analysis Code
DSMC	Direct Simulation Monte Carlo
H	Heaviside function
LEO	Low-Earth orbit
MFE	Model fit error
$\hat{\boldsymbol{n}}$	Surface normal, oriented outward
$\dot{Q}$	Total convective heat rate
r_0	RBF tuning parameter
RANGE	Ranging and Nanosatellite Guidance Experiment
RBF	Radial basis function
$\hat{\boldsymbol{t}}$	Surface tangent vector
$\hat{\boldsymbol{V}}_\infty$	Freestream velocity direction

Subscripts

A	Axial
D	Drag
L	Lift
N	Normal
p	Pressure
S	Side
T	Tangential
τ	Shear

Symbols

α	Angle of attack
β	Sideslip angle
θ	Angle of incidence
σ	Accommodation coefficient, see subscripts

*Graduate Research Assistant, Daniel Guggenheim School of Aerospace Engineering, AIAA Student Member.
†Assistant Professor, Daniel Guggenheim School of Aerospace Engineering, AIAA Senior Member.
‡David & Andrew Lewis Professor of Space Technology, Daniel Guggenheim School of Aerospace Engineering, AIAA Fellow.

I. Introduction

Satellites in low-Earth orbit (LEO) experience perturbations due to the atmosphere. One possible method for formation-keeping between two satellites is to take advantage of differences in this perturbation: differential drag.[1,2] Differential drag is highly advantageous for nanosatellite constellations because propellant or a propulsion system can be eliminated, significantly mitigating the challenge of obtaining a secondary payload launch accommodation.[3,4] One of the objectives of the Ranging and Nanosatellite Guidance Experiment (RANGE) mission is to utilize differential drag as a means of orbital formation-keeping.[5]

The standard approach to conceptual aerodynamic modeling of a satellite is to idealize the geometry and use analytic models. The assumption of a non-concave surface in the analytic approach is not valid for the geometry of a spacecraft with deployable panels, so numerical simulation is used instead. The direct simulation Monte Carlo (DSMC) approach to computational fluid dynamics (CFD) is to remove the continuum assumption on the fluid and apply gas kinetic theory.[6] The order of magnitude of the problem is reduced through simulated particles, but otherwise the mechanics of collisions, rotation, thermal motion, are included. This study used an industry standard code developed at NASA called the DSMC Analysis Code (DAC).

DSMC simulations are computationally expensive and DAC would significantly increase the runtime of a trajectory propagation tool if it were called directly from the integrator. A surrogate model for DAC was developed to solve this problem. Training and validation points for the model were selected using an iterative space-filling design.

II. Geometry Model

The RANGE mission consists of two identical nanosatellites following the CubeSat standard. Each satellite is 1.5U and has two deployable 10cm x 15cm solar panels. A SolidWorks assembly of the satellite was exported to the STL file format. The MeshLab and NetFabb Cloud tools were used to prepare the STL file for DAC, a process that involves removing the internal geometry and filling holes in the surface. The STL file used as input to DAC is shown in Figure 1. The z-axis of the satellite is nadir-pointing. These axes are fixed to the satellite and the aerodynamics are calculated with respect to these axes. The axial force coefficient (C_A) corresponds with the x-axis, side force coefficient (C_S) with the y-axis, and normal force coefficient (C_N) with the z-axis.

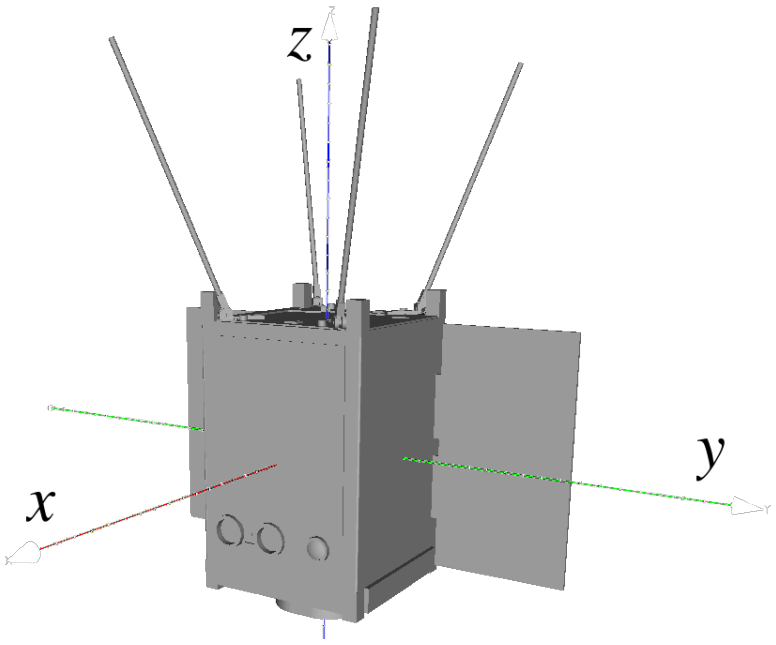

Figure 1: Geometry model for a deployed RANGE nanosatellite.

Table 1: Model values of relevant properties

Property	Symbol	Value	Units	Source
Orbit				
Altitude	h	450	km	Assumed
Speed	V_∞	7.65	km/s	Assumed circular
Satellite				
Reference length	l_{ref}	10	cm	
Reference area	A_{ref}	450	cm^2	
Surface temperature	T_W	300	K	Assumed
Atmosphere				
Density	ρ_∞	1.28×10^{-12}	kg/m^3	Ref 7
Temperature	T_∞	943	K	Ref 7
Composition	χ_{O}	0.92		Ref 7
	χ_{He}	0.05		Ref 7
	χ_{N_2}	0.03		Ref 7
Mean free path	λ	63	km	Ref 8
Mach number	M	12		Ref 8
Knudsen number	Kn	6.3×10^8		$\text{Kn} = \lambda / l_{\text{ref}}$
Molecular speed ratio	s	10.2		$s = V_\infty / \sqrt{2\,R\,T_\infty}$
Gas-Surface Interaction				
Accommodation Coefficient	σ	0.86		See Section V

III. Relevant Properties

The properties of the LEO atmosphere are sensitive to several factors including altitude, latitude, time of day, time of year, and solar activity. Table 1 provides the values of these properties that were used in developing the RANGE aerodynamic model.

IV. Free Molecular Flow Theory

This flow is classified as a free molecular based on the Mach number and Knudsen number.[9] Additionally, the high molecular speed ratio indicates that the flow is hyperthermal.[10] In these flow conditions, the aerodynamic pressure and shear coefficients of a convex geometry are given by Eqs. (1) and (2). The angle of incidence, θ, is defined as the angle between the freestream and normal directions. The tangent vector, given in Eq. (3), is parallel to the projection of the freestream vector onto the tangent plane. The contribution of $\mathrm{d}A$ to the aerodynamic force coefficients is given by $\mathrm{d}\vec{f}$ in Eq. (4), where H is the Heaviside function. The total force and moment coefficients are given by Eqs. (5) and (6).[11]

$$\lim_{s\to\infty} C_p = 2\,(2 - \sigma_N)\,\sin^2\theta \tag{1}$$

$$\lim_{s\to\infty} C_\tau = 2\,\sigma_T\,\sin\theta\cos\theta \tag{2}$$

$$\hat{\boldsymbol{t}} = \frac{\hat{\boldsymbol{n}} \times \left(\hat{\boldsymbol{V}}_\infty \times \hat{\boldsymbol{n}}\right)}{\cos\theta} \tag{3}$$

$$\mathrm{d}\vec{f} = \left(C_p\,\hat{\boldsymbol{n}} + C_\tau\,\hat{\boldsymbol{t}}\right) H(\sin\theta)\,\mathrm{d}A \tag{4}$$

$$\vec{C}_F\,A_{\text{ref}} = \oiint \mathrm{d}\vec{f} \tag{5}$$

$$\vec{C}_M \, A_{\text{ref}} \, l_{\text{ref}} = \oiint \vec{r} \times \mathrm{d}\vec{f} \tag{6}$$

V. Accommodation Coefficient

The parameters σ_N and σ_T in Eq.(4) are accommodation coefficients, which describe the average distribution of reflected velocities. Measuring these quantities independently is possible under controlled conditions, though measurements from laboratory experiments and flight data vary significantly.[12,13] The analysis of flight data assume that σ_N and σ_T are equal and the symbol σ is used instead. This is equivalent to Maxwell's description of free molecular flow, where σ represents the fraction of molecular collisions that are diffuse. The other fraction of the collisions, $1 - \sigma$, are specular, where the angle of reflection is equal to the angle of incidence, the tangential velocity is unchanged, and the normal velocity changes sign.

The analytic expressions in Section IV indicate that the magnitude of the force and moment is directly proportional to the accommodation coefficient. Since the value of this coefficient cannot be observed reliably before flight, there will be uncertainty in the aerodynamic force and moment coefficients of the RANGE nanosatellites. The accommodation coefficient for the Ariel 2 mission, which had a perigee altitude of 290 km and eccentricity of 0.07, was calculated to be 0.86.[13,14] Accommodation coefficients for satellites in the 800 - 1000 km range have been studied, however at this altitude the abundance of helium is dominant over atomic oxygen.[15] Since the atmosphere that the nanosatellites will fly through is most similar to the atmosphere experienced by Ariel 2, an accommodation coefficient of 0.86 is assumed for RANGE. Using the theory as a reference, the aerodynamics are directly proportional to σ. If the accommodation coefficient was 10% higher than this assumed value, then the aerodynamics would be 10% greater in magnitude.

VI. Direct Simulation Monte Carlo Method

The free molecular flow theory is constrained to convex geometries because it cannot model self-reflection.[16] This is the case with the RANGE nanosatellite geometry because it has deployable solar panels, so direction simulation Monte Carlo (DSMC) is used to model the flow instead. In DSMC, molecules are grouped together into simulated particles to decrease computational cost, but otherwise the fundamental conservation laws of mass, momentum, and energy are preserved.[6] NASA has developed a DSMC Analysis Code (DAC) which provides the forces, moments, and aerodynamic heating in two step process with mesh adaptation.[17] The DAC tool is used to generate the aerodynamic database for the RANGE nanosatellites.

VII. Surrogate Modeling

A. Sensitivity Analysis

A sensitivity analysis on the primary input parameters shows that the only significant factors are the orientation of the flowfield and the accommodation coefficients.[18] The accommodation coefficient is held fixed at 0.86 for reasons detailed in Section V, which leaves the flowfield orientation as the swept parameter in the surrogate model.

B. Design of Experiments

The space of all possible orientations of the flowfield, $\hat{V}_\infty$, is a unit sphere, $\mathbb{S}^2$. Baumgardner and Frederickson developed an icosahedral discretization of the sphere, which begins with an icosahedron (a 20-sided polyhedron), bisects the edges with new vertices, projects these vertices onto the unit sphere, then creates new faces from these vertices and repeats.[19] One advantage to this bisection method is that the grid is nearly-uniform across the unit sphere. The design of experiments used in this investigation starts with an octahedron and uses the same bisection and iteration process. Projection was not used in this process. Instead, in the bisection step, the unit vector of one vertex is rotated through half the angle to the joining vertex. This change simplifies the process by eliminating the need for polyhedron-to-sphere conversion.

The designs of experiments are shown in Figure 2. The red, $N = 2$, points each bisect the lines between the blue $N = 1$ points. The yellow, $N = 3$, points bisect the red points and blue points. The process can be repeated *ad infinitum*, however the number of sample points grows rapidly. The growth rate for the number

of vertices (V) is derived from the Euler characteristic and given in Eq. (7).

$$V(N) = 2 + 4^N \tag{7}$$

C. Grid Convergence

Based on the values of C_S in the third and fourth rows of aerodynamic database in the appendix, DAC is accurate to about 1%. These two runs are symmetric about the x-z plane so, in theory, the values of C_S would be equal and opposite. Since the interpolant cannot be more accurate than the training points, the grid is converged when the interpolant's percent error is on the same order of magnitude as DAC's. Shown in Figure 3 is a comparison of the distributions of errors based on the number of iterations on the octahedron. The model is trained with the points from $N \leq n$ and compared against the results from $N > n$. The octahedral design of experiments is accurate up to 50% while the next iteration is good to within 20%, and the following iteration is good to within 8%. The fourth iteration, $N = 4$ in Figures 2 and 3, is accurate to within 3.5% of the values from $N = 5$, so the grid converges at $N = 4$.

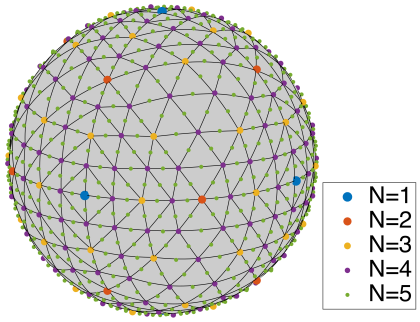

Figure 2: Sample points for iterative octahedral design of experiments.

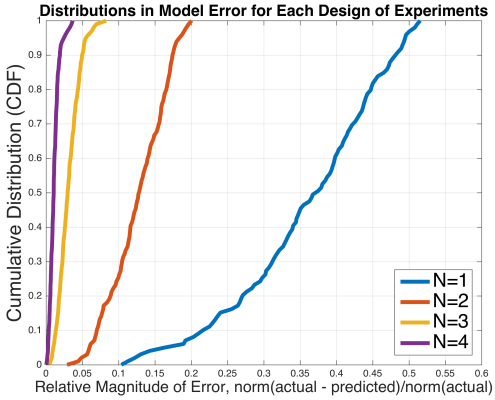

Figure 3: Error distributions for each design of experiments.

D. Interpolation Function

Interpolation of function values over the surface of a sphere applies primarily to large-scale computational meteorology.[20] In this case, the aerodynamics force vector and heat rate results from DAC are being interpolated. There are four common interpolation techniques: linear interpolation, radial basis functions (RBFs), cubic interpolation, and spherical harmonics. The RBF approach is used in this investigation because it can be tuned to maximize the fit and does not rely on gradient approximations. The two RBF kernels used in the meteorological community, thin-plate spline and multi-quadric, are both very sensitive to the value of their parameter, r_0. The inverse multiquadric RBF kernel, given in Eq. (9), is relatively insensitive to r_0 and generally yields lower errors. In this application of RBFs, the distance (r) is the angle between the points on the sphere. The construction of the interpolation function is given in Eqs. (8)-(11), where there are n training points at unit vectors $\hat{u}_i$.

$$\boldsymbol{f}\left(\hat{V}_\infty\right) \approx \hat{\boldsymbol{f}}\left(\hat{V}_\infty\right) = \sum_{i=1}^{n} \phi\left(\cos^{-1}\left(\hat{V}_\infty \cdot \hat{u}_i\right)\right) \boldsymbol{w}_i \tag{8}$$

$$\phi(r) = \frac{1}{\sqrt{r^2 + r_0^2}} \tag{9}$$

$$\Phi = \phi\left(\cos^{-1}\left(\hat{u}_i \cdot \hat{u}_j\right)\right) \quad \forall\, i, j = 1, .., n \tag{10}$$

$$\boldsymbol{w}_i = \sum_{j=1}^{n} \Phi_{ij}^{-1} \boldsymbol{f}(\hat{u}) \tag{11}$$

The training points for the RBF interpolant are a subset of all the sample points. Specifically, the training points are the vertices ($\hat{u}_j$) of the spherical triangle containing the query point ($\hat{V}_\infty$). Which triangle contains the query point is determined by checking that the point is to the left of every edge, in a counterclockwise sense. Down-selecting to three training points improves the MFE of the interpolant and decreases the computational cost for inverting the matrix Φ.

E. RBF Parameter Tuning

The parameter of the RBF, r_0, can be tuned to improve the MFE of the interpolant. Selecting the value for r_0 is the result of the optimization problem stated in Eq. (12). In this set of equations, there are m validation points. The objective function is the sum of the sample mean squared and the sample variance. The samples are the 2-norm of the difference in the validation outputs and the predicted outputs. These outputs are the three force components, the three moment components, and the aerodynamic heating, each in MKS units. Since the moments and heat rates are small, this residual is equivalent to the magnitude of the error in the force only. The 2-norm is not necessary and multi-variable statistics could be used instead. The goal is to minimize the model error and the choice of r_0 is secondary in achieving this goal compared to having enough sample points.

$$\begin{aligned} \min_{r_0} \quad & \bar{x}^2 + s^2 \\ \text{s.t.} \quad \bar{x} &= \tfrac{1}{m}\sum_{j=1}^{m} x_j \\ s^2 &= \tfrac{1}{m-1}\sum_{j=1}^{m} (x_j - \bar{x})^2 \\ x_j &= \|\boldsymbol{f}_j - \hat{\boldsymbol{f}}_j\|_2 \\ 0 &\leq r_0 \end{aligned} \tag{12}$$

The constraints in Eq. (12) are definitions for the samples, mean, and variance, and are not truly equality constraints on r_0. This is a single-objective, single-variable optimization problem with one side constraint, since ϕ is symmetric in r_0. This problem is solved by first bounding the minimum and then collapsing on the minimizer with the Golden Section Method. The minimizing value of r_0 depends on the number training points, which is determined by the number iterations, N, performed in the design of experiments.

Table 2: Tuned values of r_0

N	1	2	3	4
r_0	1.33	0.91	0.89	0.96

VIII. Validation

The DSMC simulation results become self-consistent after $N = 4$ iterations of the octahedron. Analytic models provide a basis of comparison for the simulation results, since the two have produced results within 10-15% difference in previous investigations.[11,16] In these cases, DSMC is more accurate because the analytic model is based on several assumptions of the flow and the geometry. An analytic model of the aerodynamics was developed for validation using the hyperthermal pressure and shear coefficients in Eq. (1) and (2) and the superposition methodology described in Ref 16. The outputs from DAC are compared against this model in Figures 4 and 5. There is very good agreement between the DAC outputs and the analytic model in the aerodynamic force coefficients. The analytic model is not capturing the effects of self-reflection, so there is a small deviation in these results. The moment coefficients, C_m and C_n are greatly overstated in the analytic model; flat plates near the center of reference generate very little moment. Overall, the DSMC simulation results are on the right scale and show similar trends to those in the analytic model.

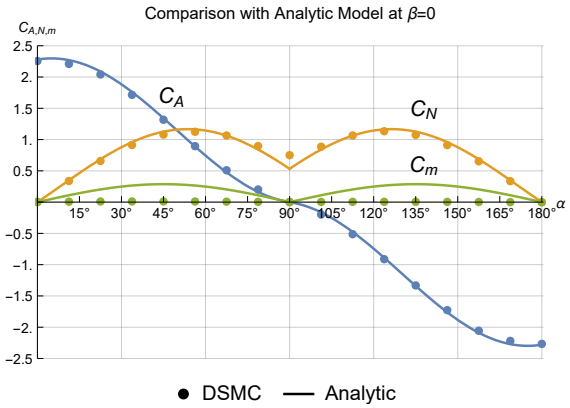

Figure 4: Comparison of DAC output with analytic model, sweeping angle of attack.

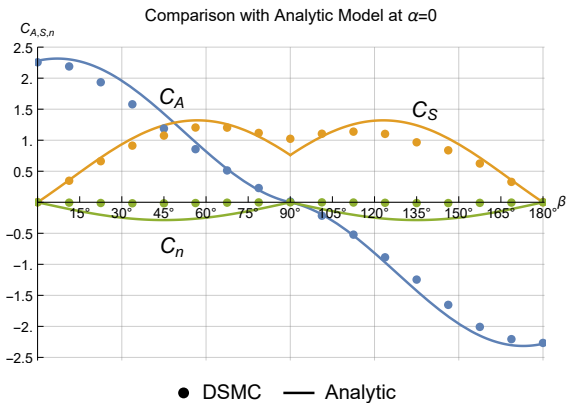

Figure 5: Comparison of DAC output with analytic model, sweeping sideslip angle.

IX. Discussion of Results

A. Drag Along the Body Axes

The aerodynamics for flow oriented along the body axes are given in the first eight rows of the aerodynamic database, in the appendix. Scaling the axial coefficients by the reference area in Table 1 gives the range of drag coefficients in Table 3. The full aerodynamic database is in the appendix and contains the body-fixed aerodynamic coefficients, the wind-frame coefficients, and the convective heating rate. The lift coefficient is the total force coefficient perpendicular to the freestream.

Table 3: Drag coefficients for flow oriented along coordinate axes

Axis	$+x$	$+y$	$+z$	$-x$	$-y$	$-z$
C_D	2.27	1.03	0.75	2.26	1.02	0.75

B. Aerodynamic Moments

The moments imparted onto the satellite are relatively small in magnitude compared to the forces, however the moments are scaled by an additional reference quantity. This makes intuition for moment coefficients difficult, especially since the magnitude of the applied torque is of interest. The order of magnitude of the freestream dynamic pressure is 10 μPa and the moment coefficients are on the order of 100 cm^3. The magnitude of the moments will be on the order of 1 nN-m, which is significantly smaller than the other torques acting on the satellite.

C. Aerodynamic Heating

In addition to the forces and moments on the satellite, DAC calculates the convective heating on the satellite, $\dot{Q}$. The heat flux distribution could be calculated in DAC post-processing, however the surface-integrated quantity is sufficiently small. The convective $\dot{Q}$ values in the aerodynamic database are between 5 and 14 mW, values that correspond to the minimum and maximum projected area.

D. Comparison with Sphere and Plate Models

The analytic geometry used in Section VIII included the multiple facets and shadowing conditions specific to the RANGE nanosatellite. Simpler analytic models, the flat plate and sphere models, are typically included in trajectory propagation tools. These models are shown against the DAC data in Figures 6 and 7. Residuals are shown in Figures 8 and 9, with the DAC results used as the reference. Neither of these models captures the trends in the aerodynamics of the RANGE nanosatellite. Using drag coefficient as a figure of merit,

the sphere and plate models differ from the DAC results by 102% and 65%, respectively and at the 80% confidence level.

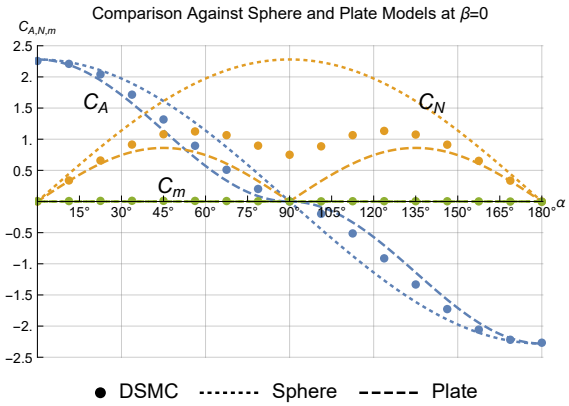

Figure 6: Comparison of DAC output with sphere and plate models, sweeping angle of attack.

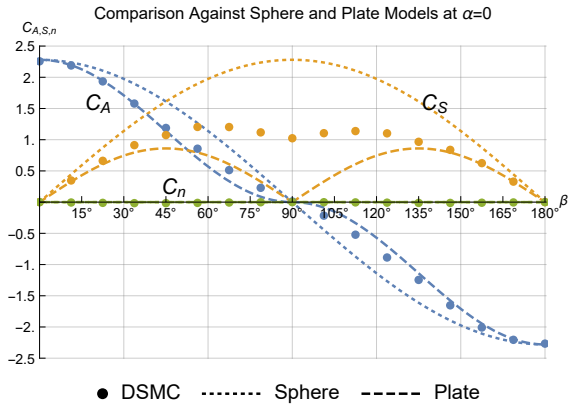

Figure 7: Comparison of DAC output with sphere and plate model, sweeping sideslip angle.

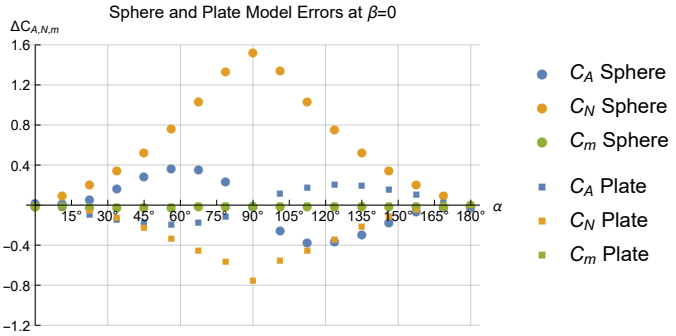

Figure 8: Sphere and plate model errors compared to DAC, sweeping angle of attack.

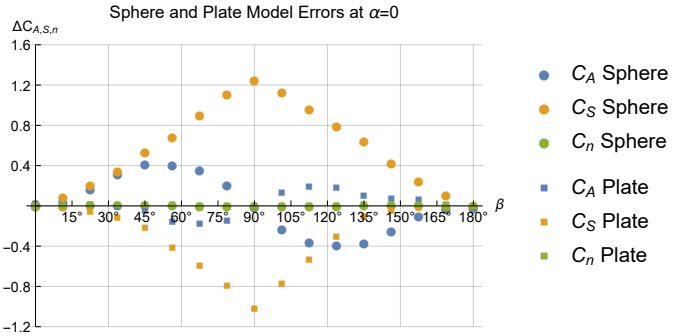

Figure 9: Sphere and plate model errors compared to DAC, sweeping sideslip angle.

X. Summary

The RANGE nanosatellites experience hyperthermal free-molecular flow in orbit. CFD in this regime requires a particle-based simulation, rather than assuming a continuum fluid. A high-fidelity aerodynamic model for these satellites is developed using the industry-standard DSMC code, DAC. A sensitivity analysis in this regime indicates that the two primary variables are the accommodation coefficient and the orientation

of the flowfield. The best estimate for the accommodation coefficient is 0.86, based on data from the Ariel 2 mission, and an aerodynamic database is compiled by sweeping across flowfield orientations.

Since DAC cannot be directly integrated into orbit propagation software, a surrogate for DAC was generated specifically for these satellites. This surrogate model applies numerical integration techniques developed in the meteorological community: using spherical geometry in the design of experiments and radial basis functions in the surrogate model. The radial basis function parameter was tuned to minimize the model error, which is approximately 3.5% relative to DAC validation runs. The DSMC sample points agree with an analytic model to within 13% on average with a worst-case error of 52%. This level of fidelity is deemed sufficient for conceptual design of the RANGE mission and much improved over use of historical sphere and plate models. In the future, this model can be incorporated into an orbit propagator and it can be compared against flight data from the RANGE mission.

References

[1]Leonard, C. L., Hollister, W. M., and Bergmann, E. V., "Orbital Formationkeeping with Differential Drag," *Journal of Guidance, Control, and Dynamics*, Vol. 12, No. 1, 1989, pp. 108–113.

[2]Varma, S. and Kumar, K. D., "Multiple Satellite Formation Flying Using Differential Aerodynamic Drag," *Journal of Spacecraft and Rockets*, Vol. 49, No. 2, 2012, pp. 325–336.

[3]Foster, C., Hallam, H., and Mason, J., "Orbit Determination and Differential-Drag Control of Planet Labs CubeSat Constellations," *AAS/AIAA Astrodynamics Specialist Conference*, Vail, CO, 2015.

[4]Gangestad, J., Rowen, D., Hardy, B., Coffman, C., and O'Brien, P., "Flight Results from AeroCube-6: A Radiation Dosimeter Mission in the 0.5U Form Factor." *12th Annual CubeSat Developers Workshop*, San Luis Obispo, CA, 2015.

[5]Gunter, B. C., Davis, B. T., Lightsey, G. E., and Braun, R. D., "The Ranging and Nanosatellite Guidance Experiment," *AIAA/USU Conference on Small Satellites*, Logan, UT, 2016.

[6]Bird, G. A., *The DSMC Method*, CreateSpace, Aug. 2013.

[7]Papitashvili, N., "NRLMSISE-00 Atmosphere Model," [Online] `http://ccmc.gsfc.nasa.gov/modelweb/models/nrlmsise00.php`, Accessed: 2015-12-11.

[8]Alexeenko, A., "Gas Dynamics Toolbox Applet," [Online] `https://web.ics.purdue.edu/~alexeenk/GDT/index.html`, July 2009, Accessed: 2015-12-11.

[9]Schaaf, S. A. and Chambré, P. L., "Flow of Rarefied Gases," Princeton University Press, Princeton, NJ, 1961.

[10]Regan, F. J. and Anandakrishnan, S. M., *Dynamics of Atmospheric Re-Entry*, American Institute of Aeronautics and Astronautics, Reston, VA, 1993.

[11]Hart, K. A., Dutta, S., Simonis, K., and Steinfeldt, B. A., "Analytically-derived Aerodynamic Force and Moment Coefficients of Resident Space Objects in Free-Molecular Flow," *AIAA Atmospheric Flight Mechanics Conference*, National Harbor, MD, Jan. 2014.

[12]Rader, D. J., Trott, W. M., Torczynski, J. R., Casteñeda, J. N., and Grasser, T. W., "Measurements of Thermal Accommodation Coefficients," Tech. Rep. SAND2005-6084, Sandia National Laboratories, Oct. 2005.

[13]Moe, K. and Moe, M. M., "Gas-Surface Interactions in Low-Earth Orbit," *International Symposium on Rarefied Gas Dynamics*, edited by D. A. Levin, I. J. Wysong, and A. L. Garcia, AIP Conference Proceedings, Pacific Grove, CA, 2011, pp. 1313–1318.

[14]Imbro, D. R., Moe, M. M., and Moe, K., "On fundamental problems in the deduction of atmospheric densities from satellite drag," *Journal of Geophysical Research*, Vol. 80, No. 22, 1975, pp. 3077–3086.

[15]Harrison, I. K. and Swinerd, G. G., "A free molecule aerodynamic investigation using multiple satellite analysis," *Planetary and Space Science*, Vol. 44, No. 2, 1996, pp. 171–180.

[16]Hart, K. A., Simonis, K. R., Steinfeldt, B. A., and Braun, R. D., "Analytical Aerodynamic Force and Moment Coefficients of Axisymmetric Objects in Rarefied Flow," *AIAA Atmospheric Flight Mechanics Conference*, Kissimmee, FL, Jan. 2015.

[17]LeBeau, G. J., "A User Guide For the DSMC Analysis Code (DAC) Software," National Aeronautics and Space Administration, 2012.

[18]Hart Jr, K. A., Steinfeldt, B. A., and Braun, R. D., "Formulation and Applications of a Probabilistic Pareto Chart," *56th AIAA/ASCE/AHS/ASC Structures, Structural Dynamics, and Materials Conference*, American Institute of Aeronautics and Astronautics, Kissimmee, FL, Jan. 2015.

[19]Baumgardner, J. R. and Frederickson, P. O., "Icosahedral Discretization of the Two-Sphere," *SIAM Journal on Numerical Analysis*, Vol. 22, No. 6, 1985, pp. 1107–1115.

[20]Carfora, M. F., "Interpolation on spherical geodesic grids: A comparative study," *Journal of Computational and Applied Mathematics*, Vol. 210, No. 1-2, 2007, pp. 99 – 105.

Appendix: Aerodynamic Database

Table 4: Aerodynamic Database

α (°)	β (°)	C_A	C_S	C_N	C_D	C_L	L/D	$\dot{Q}$ (mW)
0.00	0.00	2.256	0.000	0.000	2.256	0.000	0.000	14.10
0.00	180.00	-2.267	0.000	-0.001	2.267	0.002	0.001	14.00
0.00	-90.00	0.010	-1.034	-0.001	1.034	0.010	0.010	6.67
0.00	90.00	0.011	1.023	-0.001	1.023	0.011	0.011	6.62
-90.00	0.00	-0.000	0.000	-0.746	0.746	0.000	0.000	4.94
90.00	0.00	0.001	0.000	0.750	0.750	0.001	0.002	5.02
-45.00	0.00	1.331	-0.001	-1.086	1.709	0.173	0.101	12.10
0.00	-45.00	1.185	-1.078	-0.001	1.601	0.076	0.047	11.77
-45.00	-90.00	0.007	-0.719	-0.670	0.982	0.035	0.036	7.07
0.00	-135.00	-1.255	-0.976	0.001	1.578	0.197	0.125	11.09
-45.00	180.00	-1.323	0.001	-1.074	1.695	0.176	0.104	11.97
45.00	0.00	1.317	0.001	1.079	1.694	0.168	0.099	12.06
45.00	-90.00	0.008	-0.720	0.673	0.985	0.034	0.035	7.09
45.00	180.00	-1.332	0.001	1.074	1.702	0.182	0.107	11.99
0.00	135.00	-1.246	0.966	-0.001	1.564	0.198	0.126	10.96
-45.00	90.00	0.008	0.721	-0.673	0.986	0.035	0.035	7.09
0.00	45.00	1.188	1.074	0.000	1.600	0.081	0.050	11.74
45.00	90.00	0.007	0.714	0.669	0.978	0.033	0.033	7.03
-22.50	0.00	2.030	-0.001	-0.654	2.126	0.173	0.081	13.92
0.00	-22.50	1.916	-0.658	-0.000	2.022	0.125	0.062	13.62
-24.09	-26.57	1.627	-0.687	-0.670	1.882	0.156	0.083	13.33
22.50	0.00	2.041	0.001	0.658	2.138	0.173	0.081	14.00
24.09	-26.57	1.640	-0.692	0.678	1.898	0.156	0.082	13.47
0.00	-157.50	-2.001	-0.623	-0.001	2.087	0.190	0.091	13.41
-22.50	180.00	-2.049	-0.001	-0.659	2.145	0.176	0.082	13.94
-24.09	-153.43	-1.671	-0.644	-0.655	1.895	0.215	0.113	12.99
22.50	180.00	-2.057	0.001	0.652	2.150	0.184	0.086	13.92
24.09	-153.43	-1.675	-0.648	0.657	1.900	0.213	0.112	13.03
-67.50	-90.00	0.003	-0.331	-0.817	0.882	0.008	0.009	6.23
-67.50	0.00	0.507	-0.001	-1.066	1.179	0.061	0.051	8.53
-54.74	-45.00	0.588	-0.519	-1.045	1.305	0.061	0.047	9.79
0.00	-67.50	0.509	-1.194	0.000	1.298	0.013	0.010	9.29
-22.50	-90.00	0.009	-0.999	-0.354	1.058	0.056	0.053	7.23
-24.09	-63.43	0.582	-1.104	-0.510	1.347	0.051	0.038	10.00
-67.50	180.00	-0.512	-0.001	-1.070	1.184	0.063	0.053	8.60
-54.74	-135.00	-0.601	-0.507	-1.034	1.297	0.079	0.061	9.68
0.00	-112.50	-0.527	-1.143	-0.001	1.257	0.050	0.039	9.07
-24.09	-116.57	-0.594	-1.057	-0.499	1.309	0.070	0.054	9.75
22.50	-90.00	0.010	-1.001	0.357	1.062	0.054	0.051	7.24
24.09	-116.57	-0.593	-1.050	0.499	1.303	0.071	0.054	9.69
67.50	-90.00	0.004	-0.334	0.815	0.881	0.005	0.006	6.27
67.50	180.00	-0.512	0.001	1.065	1.180	0.066	0.056	8.57

54.74	-135.00	-0.590	-0.499	1.022	1.280	0.075	0.059	9.61
67.50	0.00	0.509	0.001	1.065	1.179	0.063	0.054	8.64
54.74	-45.00	0.583	-0.516	1.032	1.291	0.061	0.047	9.69
24.09	-63.43	0.587	-1.103	0.514	1.351	0.051	0.038	10.04
-67.50	90.00	0.004	0.326	-0.809	0.872	0.009	0.010	6.17
-54.74	135.00	-0.595	0.501	-1.034	1.292	0.075	0.058	9.64
-54.74	45.00	0.590	0.520	-1.040	1.303	0.063	0.049	9.75
0.00	22.50	1.934	0.662	0.001	2.040	0.129	0.063	13.69
24.09	26.57	1.621	0.683	0.667	1.875	0.157	0.084	13.26
-22.50	90.00	0.010	0.977	-0.351	1.037	0.050	0.049	7.13
0.00	67.50	0.513	1.203	0.000	1.308	0.013	0.010	9.37
-24.09	63.43	0.589	1.111	-0.516	1.358	0.052	0.038	10.11
-24.09	26.57	1.633	0.693	-0.672	1.891	0.156	0.082	13.36
0.00	157.50	-2.008	0.625	-0.000	2.095	0.192	0.091	13.47
24.09	153.43	-1.675	0.648	0.659	1.902	0.212	0.112	13.04
-24.09	153.43	-1.670	0.645	-0.652	1.893	0.216	0.114	12.96
-24.09	116.57	-0.596	1.057	-0.498	1.310	0.073	0.056	9.75
0.00	112.50	-0.522	1.138	0.000	1.251	0.047	0.037	9.02
67.50	90.00	0.004	0.328	0.812	0.876	0.008	0.010	6.17
54.74	135.00	-0.588	0.497	1.017	1.273	0.075	0.059	9.54
24.09	116.57	-0.592	1.046	0.496	1.298	0.072	0.055	9.66
22.50	90.00	0.010	0.980	0.349	1.039	0.054	0.052	7.12
54.74	45.00	0.592	0.524	1.046	1.310	0.063	0.048	9.87
24.09	63.43	0.588	1.113	0.516	1.359	0.052	0.038	10.06
-12.05	-65.56	0.568	-1.198	-0.253	1.349	0.037	0.027	9.83
-12.20	-53.79	0.917	-1.162	-0.291	1.507	0.061	0.040	11.16
0.00	-56.25	0.837	-1.177	-0.001	1.443	0.042	0.029	10.61
0.00	-78.75	0.230	-1.113	0.000	1.136	0.009	0.008	7.74
-11.25	-90.00	0.011	-1.027	-0.172	1.041	0.034	0.032	6.91
-11.46	-78.30	0.236	-1.107	-0.196	1.149	0.033	0.029	7.93
-23.87	-76.80	0.256	-1.047	-0.425	1.158	0.049	0.042	8.27
12.20	-53.79	0.913	-1.159	0.288	1.502	0.060	0.040	11.11
12.05	-65.56	0.566	-1.191	0.253	1.342	0.036	0.027	9.77
11.25	-90.00	0.011	-1.025	0.170	1.039	0.035	0.034	6.87
11.46	-78.30	0.241	-1.122	0.202	1.164	0.032	0.027	8.09
23.87	-76.80	0.258	-1.050	0.430	1.162	0.046	0.039	8.36
-12.20	-126.21	-0.955	-1.076	-0.278	1.458	0.138	0.095	10.65
-12.05	-114.44	-0.579	-1.137	-0.246	1.298	0.062	0.048	9.50
0.00	-123.75	-0.882	-1.094	-0.001	1.399	0.126	0.090	10.14
0.00	-101.25	-0.215	-1.092	-0.000	1.113	0.003	0.002	7.66
-11.46	-101.70	-0.228	-1.093	-0.199	1.134	0.027	0.024	7.93
-23.87	-103.20	-0.250	-1.041	-0.425	1.151	0.045	0.039	8.32
12.05	-114.44	-0.572	-1.124	0.245	1.283	0.061	0.047	9.43
12.20	-126.21	-0.944	-1.067	0.277	1.445	0.134	0.093	10.57
11.46	-101.70	-0.222	-1.079	0.194	1.118	0.029	0.025	7.80
23.87	-103.20	-0.244	-1.020	0.418	1.128	0.042	0.037	8.14
-56.25	0.00	0.901	-0.000	-1.137	1.446	0.117	0.081	10.55

-52.06	-20.10	0.969	-0.298	-1.126	1.511	0.119	0.079	11.07
-62.91	-27.30	0.568	-0.250	-1.096	1.258	0.065	0.052	9.29
-11.25	0.00	2.227	-0.000	-0.339	2.251	0.102	0.046	14.24
0.00	-11.25	2.178	-0.348	0.000	2.204	0.084	0.038	14.19
-11.46	-11.70	2.131	-0.356	-0.344	2.184	0.124	0.057	14.28
-35.26	-15.00	1.582	-0.349	-0.941	1.865	0.181	0.097	13.12
-39.76	-33.69	1.120	-0.650	-0.962	1.609	0.119	0.074	11.92
-33.75	0.00	1.733	0.000	-0.919	1.951	0.199	0.102	13.31
-23.87	-13.20	1.902	-0.365	-0.690	2.048	0.171	0.084	13.87
-25.24	-45.00	1.079	-0.974	-0.622	1.578	0.094	0.059	11.76
-39.76	-56.31	0.622	-0.862	-0.832	1.348	0.056	0.042	10.17
-12.05	-24.44	1.837	-0.702	-0.350	1.993	0.138	0.069	13.74
-12.20	-36.21	1.472	-0.945	-0.331	1.777	0.116	0.065	12.79
0.00	-33.75	1.593	-0.917	-0.002	1.834	0.122	0.067	13.00
-35.26	15.00	1.576	0.348	-0.937	1.858	0.181	0.097	13.08
-23.87	13.20	1.917	0.366	-0.695	2.065	0.174	0.084	13.97
-52.06	-159.90	-0.987	-0.288	-1.126	1.519	0.136	0.089	11.05
-56.25	180.00	-0.907	0.000	-1.128	1.442	0.128	0.089	10.46
-62.91	-152.70	-0.575	-0.245	-1.093	1.257	0.074	0.059	9.23
-78.75	-90.00	0.000	-0.147	-0.789	0.803	0.009	0.012	5.45
-78.75	0.00	0.202	-0.000	-0.901	0.923	0.023	0.025	6.49
-73.68	-45.00	0.215	-0.181	-0.921	0.963	0.026	0.027	6.87
-62.91	-62.70	0.243	-0.420	-0.931	1.050	0.025	0.024	7.71
-78.75	180.00	-0.200	-0.001	-0.888	0.910	0.023	0.025	6.39
-73.68	-135.00	-0.213	-0.181	-0.927	0.968	0.024	0.025	6.90
-62.91	-117.30	-0.242	-0.414	-0.933	1.048	0.025	0.024	7.69
0.00	-168.75	-2.218	-0.332	-0.002	2.240	0.107	0.048	14.06
-11.25	180.00	-2.221	-0.001	-0.336	2.244	0.104	0.046	14.09
-11.46	-168.30	-2.177	-0.340	-0.344	2.225	0.148	0.066	14.13
-35.26	-165.00	-1.596	-0.335	-0.937	1.870	0.197	0.105	12.98
-39.76	-146.31	-1.136	-0.607	-0.933	1.582	0.162	0.103	11.51
-33.75	180.00	-1.729	-0.000	-0.912	1.944	0.202	0.104	13.14
-23.87	-166.80	-1.938	-0.349	-0.686	2.076	0.197	0.095	13.77
-39.76	-123.69	-0.645	-0.831	-0.820	1.332	0.086	0.065	10.06
-25.24	-135.00	-1.125	-0.896	-0.597	1.547	0.177	0.114	11.25
-12.05	-155.56	-1.900	-0.654	-0.341	2.027	0.209	0.103	13.31
-12.20	-143.79	-1.522	-0.851	-0.313	1.758	0.221	0.126	12.06
0.00	-146.25	-1.642	-0.838	0.000	1.831	0.215	0.118	12.37
52.06	-20.10	0.964	-0.299	1.123	1.506	0.116	0.077	11.11
56.25	0.00	0.895	-0.000	1.124	1.432	0.119	0.083	10.45
62.91	-27.30	0.569	-0.253	1.098	1.260	0.065	0.051	9.33
52.06	20.10	0.963	0.298	1.116	1.499	0.119	0.080	11.04
62.91	27.30	0.575	0.254	1.107	1.271	0.066	0.052	9.41
-25.24	45.00	1.084	0.975	-0.625	1.583	0.095	0.060	11.78
-12.20	53.79	0.904	1.147	-0.285	1.486	0.060	0.040	11.02
-12.20	36.21	1.479	0.946	-0.334	1.783	0.119	0.067	12.88
56.25	180.00	-0.912	0.001	1.133	1.449	0.129	0.089	10.54
52.06	-159.90	-0.977	-0.285	1.112	1.501	0.135	0.090	10.94

62.91	-152.70	-0.566	-0.242	1.072	1.234	0.073	0.059	9.13
78.75	0.00	0.201	0.000	0.896	0.918	0.023	0.025	6.48
78.75	-90.00	0.001	-0.149	0.795	0.809	0.009	0.011	5.49
73.68	-45.00	0.216	-0.184	0.931	0.973	0.024	0.025	6.98
62.91	-62.70	0.242	-0.416	0.922	1.040	0.026	0.025	7.65
78.75	180.00	-0.198	-0.000	0.886	0.907	0.021	0.024	6.42
73.68	-135.00	-0.211	-0.179	0.908	0.949	0.024	0.026	6.84
62.91	-117.30	-0.239	-0.412	0.919	1.035	0.024	0.023	7.69
11.25	180.00	-2.220	-0.001	0.335	2.242	0.105	0.047	14.07
11.46	-168.30	-2.168	-0.340	0.340	2.216	0.148	0.067	14.11
35.26	-15.00	1.591	-0.350	0.949	1.876	0.180	0.096	13.16
39.76	-33.69	1.126	-0.651	0.965	1.615	0.121	0.075	11.97
39.76	-56.31	0.630	-0.866	0.837	1.358	0.060	0.044	10.25
25.24	-45.00	1.074	-0.970	0.623	1.573	0.090	0.058	11.74
12.20	-36.21	1.453	-0.926	0.327	1.749	0.119	0.068	12.63
12.05	-24.44	1.854	-0.708	0.352	2.011	0.141	0.070	13.85
-39.76	56.31	0.630	0.867	-0.837	1.359	0.060	0.044	10.26
-39.76	33.69	1.119	0.648	-0.960	1.606	0.120	0.075	11.92
-52.06	20.10	0.975	0.303	-1.143	1.528	0.114	0.074	11.23
-62.91	27.30	0.571	0.252	-1.098	1.261	0.067	0.053	9.33
-35.26	-105.00	-0.255	-0.918	-0.625	1.139	0.041	0.036	8.39
-33.75	-90.00	0.009	-0.878	-0.523	1.021	0.054	0.053	7.25
-52.06	-110.10	-0.254	-0.634	-0.853	1.093	0.024	0.022	8.16
-56.25	-90.00	0.006	-0.533	-0.777	0.942	0.013	0.014	6.82
-35.26	-75.00	0.263	-0.926	-0.627	1.148	0.047	0.041	8.42
-52.06	-69.90	0.253	-0.634	-0.846	1.087	0.027	0.025	8.06
-12.05	65.56	0.561	1.186	-0.251	1.336	0.035	0.026	9.73
0.00	56.25	0.856	1.205	0.000	1.477	0.043	0.029	10.82
33.75	0.00	1.715	-0.000	0.914	1.934	0.193	0.100	13.21
23.87	-13.20	1.918	-0.366	0.693	2.065	0.176	0.085	13.95
11.25	0.00	2.209	0.001	0.338	2.233	0.100	0.045	14.19
11.46	-11.70	2.123	-0.354	0.343	2.176	0.124	0.057	14.19
35.26	-105.00	-0.251	-0.896	0.616	1.115	0.036	0.032	8.23
33.75	-90.00	0.010	-0.882	0.530	1.028	0.050	0.049	7.27
39.76	-123.69	-0.638	-0.825	0.814	1.320	0.083	0.063	10.00
52.06	-110.10	-0.248	-0.624	0.840	1.075	0.023	0.021	8.04
56.25	-90.00	0.006	-0.527	0.771	0.934	0.012	0.013	6.76
35.26	-75.00	0.263	-0.920	0.621	1.140	0.048	0.042	8.35
52.06	-69.90	0.255	-0.640	0.856	1.098	0.026	0.024	8.15
0.00	168.75	-2.206	0.328	0.000	2.228	0.108	0.049	13.97
11.46	168.30	-2.165	0.340	0.341	2.213	0.147	0.066	14.14
-11.46	168.30	-2.157	0.336	-0.340	2.204	0.148	0.067	14.02
25.24	-135.00	-1.117	-0.896	0.596	1.542	0.170	0.110	11.23
39.76	-146.31	-1.151	-0.611	0.936	1.596	0.170	0.107	11.61
12.05	-155.56	-1.884	-0.652	0.338	2.012	0.204	0.102	13.30
23.87	-166.80	-1.934	-0.349	0.684	2.072	0.197	0.095	13.74
12.20	-143.79	-1.520	-0.853	0.313	1.757	0.218	0.124	12.09
35.26	-165.00	-1.584	-0.329	0.922	1.851	0.202	0.109	12.81

33.75	180.00	-1.727	-0.000	0.912	1.943	0.201	0.104	13.20
-11.25	90.00	0.009	1.033	-0.171	1.047	0.035	0.033	6.92
0.00	78.75	0.229	1.117	-0.000	1.141	0.007	0.006	7.78
-11.46	78.30	0.240	1.114	-0.200	1.157	0.031	0.027	8.01
-23.87	76.80	0.259	1.052	-0.427	1.163	0.049	0.042	8.35
-52.06	159.90	-0.980	0.285	-1.113	1.504	0.137	0.091	10.95
-62.91	152.70	-0.574	0.243	-1.093	1.257	0.073	0.058	9.22
35.26	15.00	1.594	0.352	0.951	1.880	0.180	0.096	13.22
39.76	33.69	1.117	0.651	0.961	1.607	0.117	0.073	11.93
23.87	13.20	1.896	0.362	0.688	2.042	0.171	0.084	13.81
52.06	159.90	-0.984	0.287	1.112	1.506	0.141	0.093	10.99
62.91	152.70	-0.572	0.243	1.094	1.256	0.071	0.057	9.22
0.00	123.75	-0.887	1.102	-0.001	1.409	0.125	0.089	10.21
12.20	126.21	-0.941	1.058	0.273	1.435	0.138	0.096	10.49
12.05	114.44	-0.573	1.122	0.246	1.282	0.062	0.048	9.43
-12.20	126.21	-0.941	1.059	-0.274	1.437	0.137	0.095	10.47
-12.05	114.44	-0.572	1.132	-0.245	1.290	0.059	0.045	9.42
0.00	101.25	-0.216	1.105	-0.001	1.126	0.003	0.003	7.71
-11.46	101.70	-0.224	1.088	-0.198	1.128	0.027	0.024	7.87
-23.87	103.20	-0.247	1.042	-0.425	1.151	0.044	0.038	8.27
11.25	90.00	0.011	1.035	0.172	1.048	0.035	0.033	6.97
11.46	78.30	0.240	1.115	0.201	1.158	0.031	0.027	8.02
11.46	101.70	-0.225	1.096	0.197	1.135	0.029	0.026	7.89
23.87	103.20	-0.242	1.023	0.420	1.131	0.042	0.037	8.18
-12.20	143.79	-1.533	0.857	-0.316	1.771	0.222	0.126	12.17
-25.24	135.00	-1.118	0.903	-0.599	1.548	0.167	0.108	11.29
0.00	146.25	-1.653	0.837	0.000	1.840	0.222	0.121	12.37
-12.05	155.56	-1.903	0.657	-0.343	2.032	0.206	0.101	13.40
-23.87	166.80	-1.928	0.348	-0.685	2.066	0.194	0.094	13.74
-39.76	123.69	-0.638	0.821	-0.812	1.317	0.085	0.064	9.94
-39.76	146.31	-1.151	0.610	-0.940	1.597	0.169	0.106	11.62
-35.26	165.00	-1.604	0.333	-0.936	1.876	0.203	0.108	12.99
-78.75	90.00	0.002	0.145	-0.778	0.792	0.010	0.013	5.39
-73.68	45.00	0.216	0.185	-0.933	0.975	0.024	0.025	6.96
-62.91	62.70	0.242	0.415	-0.920	1.038	0.026	0.025	7.64
-73.68	135.00	-0.216	0.185	-0.940	0.982	0.023	0.024	6.99
-62.91	117.30	-0.239	0.411	-0.921	1.037	0.024	0.023	7.60
0.00	33.75	1.579	0.913	0.000	1.820	0.118	0.065	12.92
12.20	36.21	1.466	0.940	0.330	1.769	0.117	0.066	12.78
12.05	24.44	1.839	0.698	0.348	1.992	0.143	0.072	13.68
-12.05	24.44	1.836	0.699	-0.348	1.990	0.141	0.071	13.68
0.00	11.25	2.189	0.347	-0.001	2.215	0.087	0.039	14.14
11.46	11.70	2.117	0.353	0.343	2.170	0.123	0.057	14.18
-11.46	11.70	2.113	0.354	-0.342	2.166	0.122	0.056	14.16
35.26	165.00	-1.603	0.333	0.933	1.873	0.205	0.109	13.01
23.87	166.80	-1.922	0.347	0.681	2.059	0.195	0.095	13.68
39.76	146.31	-1.153	0.615	0.939	1.600	0.169	0.106	11.63
12.05	155.56	-1.892	0.653	0.338	2.019	0.207	0.102	13.28

39.76	123.69	-0.640	0.827	0.818	1.325	0.083	0.063	10.02
25.24	135.00	-1.124	0.903	0.602	1.553	0.169	0.109	11.31
12.20	143.79	-1.528	0.861	0.317	1.769	0.216	0.122	12.18
78.75	90.00	0.003	0.146	0.787	0.801	0.011	0.013	5.52
73.68	135.00	-0.214	0.181	0.921	0.962	0.025	0.026	6.90
62.91	117.30	-0.240	0.413	0.925	1.041	0.024	0.023	7.66
73.68	45.00	0.218	0.185	0.930	0.972	0.026	0.027	6.99
62.91	62.70	0.245	0.420	0.933	1.052	0.026	0.025	7.73
39.76	56.31	0.632	0.872	0.842	1.366	0.059	0.043	10.34
25.24	45.00	1.073	0.971	0.622	1.572	0.090	0.057	11.71
12.05	65.56	0.564	1.191	0.252	1.342	0.035	0.026	9.76
23.87	76.80	0.259	1.051	0.429	1.163	0.047	0.041	8.36
12.20	53.79	0.901	1.146	0.288	1.485	0.057	0.038	10.99
-35.26	105.00	-0.254	0.906	-0.620	1.126	0.038	0.034	8.33
-33.75	90.00	0.008	0.888	-0.530	1.033	0.053	0.051	7.30
-52.06	110.10	-0.251	0.628	-0.843	1.081	0.025	0.023	8.05
-56.25	90.00	0.006	0.531	-0.771	0.936	0.015	0.016	6.73
-35.26	75.00	0.262	0.921	-0.623	1.141	0.046	0.041	8.40
-52.06	69.90	0.258	0.640	-0.851	1.095	0.030	0.028	8.15
52.06	69.90	0.258	0.643	0.853	1.098	0.031	0.028	8.21
56.25	90.00	0.007	0.528	0.769	0.933	0.013	0.014	6.75
35.26	75.00	0.265	0.928	0.630	1.152	0.045	0.039	8.46
33.75	90.00	0.009	0.880	0.532	1.027	0.048	0.046	7.27
35.26	105.00	-0.249	0.891	0.614	1.110	0.035	0.031	8.20
52.06	110.10	-0.246	0.624	0.842	1.076	0.020	0.018	8.04